New Journal of Physics
The open access journal at the forefront of physics

Deutsche Physikalische Gesellschaft DPG IOP Institute of Physics

PAPER • OPEN ACCESS

Measuring and modeling polymer concentration profiles near spindle boundaries argues that spindle microtubules regulate their own nucleation

To cite this article: Bryan Kaye *et al* 2018 *New J. Phys.* **20** 055012

View the article online for updates and enhancements.

Related content

- Collective behavior of minus-ended motors in mitotic microtubule asters gliding toward DNA
Chaitanya A Athale, Ana Dinarina, Francois Nedelec et al.

- Model of turnover kinetics in the lamellipodium: implications of slow- and fast- diffusing capping protein and Arp2/3 complex
Laura M McMillen and Dimitrios Vavylonis

- pawFLIM: reducing bias and uncertainty to enable lower photon count in FLIM experiments
Mauro Silberberg and Hernán E Grecco

This content was downloaded from IP address 128.122.80.249 on 29/05/2018 at 22:48

New Journal of Physics
The open access journal at the forefront of physics

Deutsche Physikalische Gesellschaft DPG
IOP Institute of Physics

Published in partnership with: Deutsche Physikalische Gesellschaft and the Institute of Physics

OPEN ACCESS

RECEIVED
23 October 2017

REVISED
24 March 2018

ACCEPTED FOR PUBLICATION
4 May 2018

PUBLISHED
25 May 2018

Original content from this work may be used under the terms of the Creative Commons Attribution 3.0 licence.

Any further distribution of this work must maintain attribution to the author(s) and the title of the work, journal citation and DOI.

PAPER

Measuring and modeling polymer concentration profiles near spindle boundaries argues that spindle microtubules regulate their own nucleation

Bryan Kaye[1,2], Olivia Stiehl[1,2], Peter J Foster[1,2,6], Michael J Shelley[3,4], Daniel J Needleman[1,2,5] and Sebastian Fürthauer[4]

[1] John A. Paulson School of Engineering and Applied Science, Harvard University, Cambridge, MA 02138, United States of America
[2] FAS Center for Systems Biology, Harvard University, Cambridge, MA 02138, United States of America
[3] Courant Institute, NYU, New York, NY 10012, United States of America
[4] Center for Computational Biology, Flatiron Institute, New York, NY 10010, United States of America
[5] Department of Molecular and Cellular Biology, Harvard University, Cambridge, MA 02138, United States of America
[6] Present address: Physics of Livings Systems, Department of Physics, Massachusetts Institute of Technology, Cambridge, MA 02139, United States of America.

Keywords: cell division, microtubule nucleation, spindle, self assembly

Abstract

Spindles are self-organized microtubule-based structures that segregate chromosomes during cell division. The mass of the spindle is controlled by the balance between microtubule turnover and nucleation. The mechanisms that control the spatial regulation of microtubule nucleation remain poorly understood. While previous work found that microtubule nucleators bind to pre-existing microtubules in the spindle, it is still unclear whether this binding regulates the activity of those nucleators. Here we use a combination of experiments and mathematical modeling to investigate this issue. We measured the concentration of microtubules and soluble tubulin in and around the spindle. We found a very sharp decay in the concentration of microtubules at the spindle interface. This is inconsistent with a model in which the activity of nucleators is independent of their association with microtubules but consistent with a model in which microtubule nucleators are only active when bound to pre-existing microtubules. This argues that the activity of microtubule nucleators is greatly enhanced when bound to pre-existing microtubules. Thus, microtubule nucleators are both localized and activated by the microtubules they generate.

1. Introduction

The spindle is a self-organized cellular structure which separates chromosomes during cell division. In meiotic *Xenopus* egg extract spindles, the spatial regulation of microtubule nucleation is crucial for establishing spindle architecture (Brugués *et al* 2012, Wieczorek *et al* 2015, Oh *et al* 2016, Decker *et al* 2018). The Ran pathway, the same pathway used in interphase for nuclear import, promotes microtubule nucleation near chromosomes by activating spindle assembly factors (Kalab *et al* 1999, Ohba *et al* 1999, Zhang *et al* 1999, Kalab *et al* 2002, Maresca *et al* 2009, Hasegawa *et al* 2013). Many of these spindle assembly factors bind to microtubules (Roll-Mecak and Vale 2006, Ho *et al* 2011, Kamasaki *et al* 2013, Petry *et al* 2013, Hsia *et al* 2014, Wieczorek *et al* 2015, Oh *et al* 2016). Outside of the spindle in *Xenopus* egg extracts, where individual microtubules can be visualized, it has been found that nucleators, and the microtubules which grow from them, localize to other microtubules in a 'branching' pattern (Petry *et al* 2013). Branching nucleation has been invoked to explain the size and mass of spindles (Oh *et al* 2016, Decker *et al* 2018), as well as other microtubule-based structures such as interphase asters in *Xenopus* eggs (Ishihara *et al* 2014, Ishihara *et al* 2016). While this work demonstrates that nucleators can bind to pre-existing microtubules, it remains unknown whether this binding stimulates the activity of nucleators or merely localizes them to the spindle.

© 2018 The Author(s). Published by IOP Publishing Ltd on behalf of Deutsche Physikalische Gesellschaft

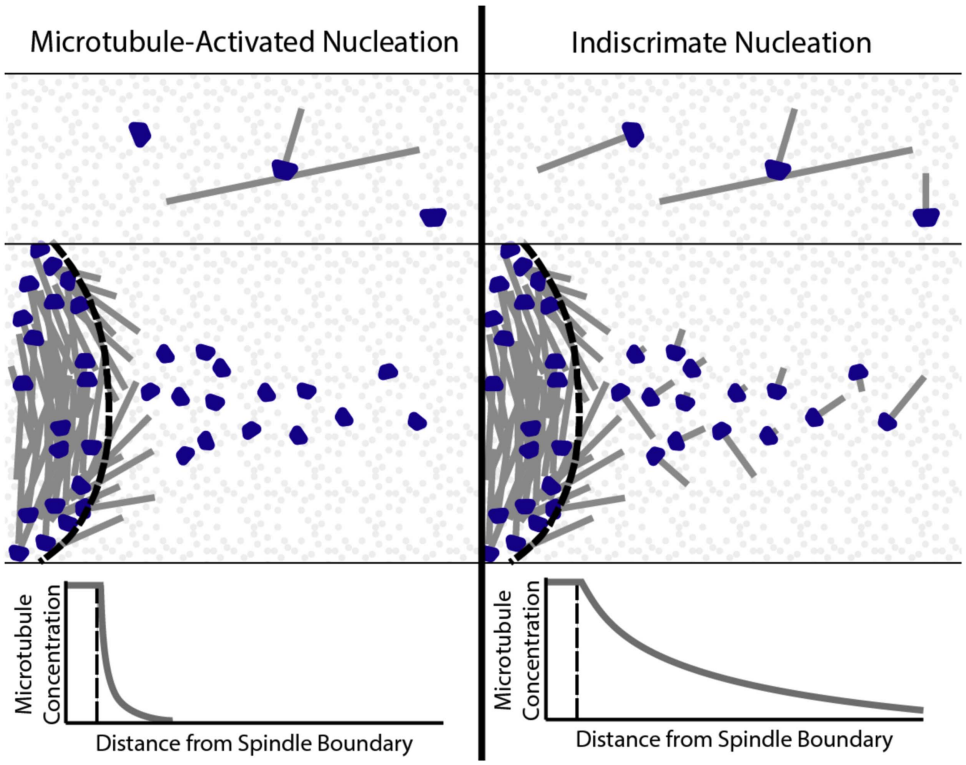

Figure 1. (Top) Schematic representation of two extreme scenarios of nucleation. In the microtubule-activated nucleation scenario, nucleators can only nucleate when bound to pre-existing microtubules. In the indiscriminate nucleation scenario, nucleator activity is not affected by other microtubules. (Middle) Schematic representation of the spindle, which has a soft boundary and nucleators diffusing away from the spindle boundary. (Bottom) In the microtubule activated nucleation scenario, the gradient of microtubules diffusing out of the spindle sets the interface width. In the indiscriminate nucleation scenario, nucleators continue to create microtubules as they diffuse away from the spindle. This predicts a much wider microtubule concentration profile at the spindle interface.

In the present paper, we address this question by measuring the concentration profile of microtubules and free tubulin monomers near the spindle boundary. By quantifying the decay of microtubule concentration around this interface between the spindle and the cytoplasm which surrounds it, we can distinguish between two possible scenarios for how nucleators work. In the first scenario, taken in its extreme form, nucleators can only create new microtubules when bound to pre-existing microtubules, while in the second, nucleator activity is unaffected by being bound to a pre-existing microtubule (see figure 1, top). We show that near the boundary of the spindle, where the concentration of microtubules drops, the difference in nucleator and microtubule diffusion rates would result in a zone in which concentrations of microtubules and nucleators would vary substantially, allowing us to ask which of the two scenarios better explains the data and thus is more likely correct.

To do this, we first quantified the concentration profile of microtubules near the spindle boundary. Since the concentration of monomeric tubulin near the spindle boundary was likely to have spatial gradients, we could not rely on fluorescence microscopy alone to determine the polymer concentration profile. Instead, we used a fluorescence lifetime imaging microscopy (FLIM)-Förster resonance energy transfer (FRET) based technique (Kaye *et al* 2017a), which allows separate measurements of the concentration profiles of microtubule and tubulin monomer density. Using this technique, we found that the microtubule concentration decreases sharply around the spindle.

To interpret these data, we developed a 1D mathematical model for the concentration of microtubules as a function of distance from the interface of the *Xenopus* metaphase spindle. Since microtubules move relatively slowly ($\simeq 2\ \mu$m min^{-1}) and mostly parallel to the spindle boundary and turn over rapidly with a lifetime of $\simeq$20 s (Sawin 1991, Needleman *et al* 2010), our model neglects transport and only considers the reaction diffusion dynamics of microtubules and nucleators. This simple model shows clear cut and testable differences between the two nucleation scenarios which we wanted to distinguish. If nucleators must be bound to pre-existing microtubules to nucleate, then our model predicts a sharp decay of the microtubule concentration at the spindle boundary set by the distance microtubules diffuse before they depolymerize (figure 1, left). If, in contrast, nucleator activity was unaffected by binding to pre-existing microtubules, the model predicts the width of the microtubule concentration profile at the spindle boundary to be broader because of the diffusion of

nucleators (figure 1, right). By comparing the expectations from the model to experimental results, we argue that nucleators are activated by binding to pre-existing microtubules. This finding demonstrates that the spindle, which turns over rapidly and has no enclosing membrane, maintains a sharp interface by a feedback mechanism between the nucleator and its nucleation product.

The structure of our paper is as follows: in section 2 we give an overview of the technique used to measure microtubule mass and show that the microtubule concentration profile decays quickly away from the spindle. We also show that the shape of the interface is very similar from spindle to spindle and does not depend on the position along the circumference of the spindle. In section 3 we outline the key ideas underlying our study and formulate a description of the reaction-diffusion dynamics that shape the spindle interface. We then combine theory and experiment to demonstrate that the shape of the spindle interface is consistent with nucleators being activated by binding to pre-existing microtubules, but inconsistent with nucleators indiscriminately nucleating microtubules. Finally, in section 4 we consider the implications of these findings for our understanding of the spindle and other organelles.

2. Measuring microtubule concentration near the spindle interface

We sought to test competing models of microtubule nucleation by measuring the concentration profile of microtubules near the spindle interface. We now describe how we performed these measurements and present the results.

2.1. FLIM-FRET

To measure the microtubule concentration profile near the spindle interface, we needed a technique that could measure polymer concentration independently of monomer concentration. If fluorescence microscopy were able to visualize each individual filament, then it alone could be used to measure the concentration of polymer. However, it is not possible to directly visualize individual microtubules in and around spindles because of their high density and the large background signal from soluble tubulin. A possible alternative approach for using fluorescence microscopy to measure microtubule concentration is to note that the fluorescence signal in each pixel is proportional to the total amount of labeled tubulin, which is the sum of soluble tubulin and tubulin in microtubules, in the voxel corresponding to that pixel. Thus, if the fluorescence from soluble tubulin at every pixel were known, it could be subtracted from the total fluorescence, revealing the concentration of microtubules. Using this approach requires an estimate of the soluble concentration of tubulin, which might be obtained by measuring the fluorescence intensity far away from the spindle. However, this procedure is only valid if the concentration of microtubules far from the spindle is negligible and if the concentration of soluble tubulin is spatially uniform. It is not clear that either assumption is valid. The concentration of soluble tubulin could be depleted in spindles, because of extensive microtubule polymerization, or on the contrary be enriched, due to complex interactions between tubulin monomers and microtubules. Thus, standard fluorescence microscopy cannot be used to measure the spatial variation in microtubule concentration at the spindle interface. To overcome these challenges, we use both fluorescence microscopy and spectroscopy to determine the concentration of microtubules in each pixel without making any assumptions about the spatial distribution of soluble tubulin or concentration of microtubules far from the spindle.

We use the method introduced by Kaye *et al* (2017a) to measure microtubule concentration. We provide a brief summary here: the measurement system relies on FLIM in the presence of two subpopulations of fluorophores which can engage in FRET. Populations of tubulin, labeled with either donor or acceptor fluorophores, are added to *Xenopus* egg extract. FRET can occur when a donor and acceptor are within ≈5 nm of each other. This is exceedingly rare in solution. In contrast, when the labeled tubulin is incorporated into microtubules, the microtubule lattice localizes donors and acceptors together and FRET becomes more likely.

To measure the subpopulation of donors engaged in FRET and the subpopulation of donors not engaged in FRET, we use time-domain FLIM. To make FLIM measurements, the donor fluorophores are put into an excited state by a laser pulse and relax back to their ground state either by emitting a photon or by dissipating the energy as heat. The amount of time spent in the excited state is called the fluorescence lifetime. If an acceptor is nearby, an additional pathway of relaxation, FRET, is available, shortening the amount of time the donors spend in an excited state (figure 2(A)) and thus shortening the fluorescence lifetime. If there is a subpopulation of donors engaged in FRET and a subpopulation not engaged in FRET, the measured photon emission will be the weighted sum of the photon emission from each subpopulation (figure 2(B)), where the weights are given by the number of donors in each subpopulation. Thus, these weights can be deduced by analyzing the photon emission from a sample with both subpopulations, allowing the fraction of donors engaged in FRET to be measured, from which the fraction of donors in microtubules can be calculated.

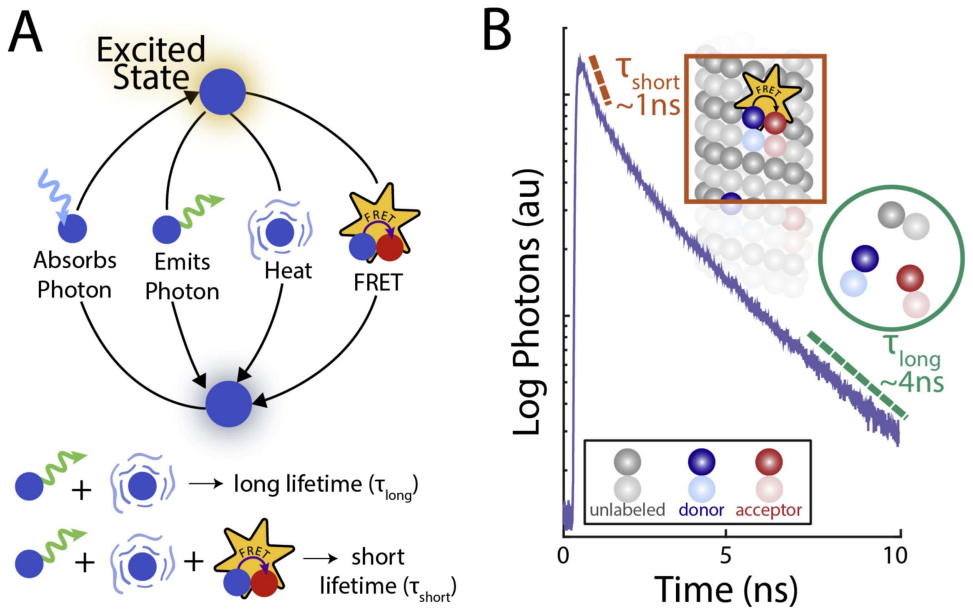

Figure 2. FLIM measurements of FRET reveal the fraction of tubulin in polymer. (A) Diagram of the excitation and relaxation pathways of donor fluorophores (blue). If a donor fluorophore absorbs an incoming photon, it is raised into an excited state. The fluorophore relaxes back to the ground state by either emitting a photon or releasing heat. When an acceptor is nearby, FRET can occur, providing an additional pathway for the donor fluorophore to relax. Thus, the average time the fluorophore spends in an excited state, referred to as the lifetime, is shorter when the fluorophore is engaged in FRET. (B) Photon emission measurements, provided by FLIM, reveal the fraction of tubulin in polymer. Soluble donor-fluorophore-labeled tubulin is very unlikely to be close enough to an acceptor to be engaged in FRET and thus produces a long-lifetime photon emission. Donor-labeled tubulin in microtubules that are near acceptor-labeled tubulin produce a short-lifetime photon emission. By analyzing the photon emission curves, we can measure the ratio of tubulin in microtubules to soluble tubulin. Figure adapted from Kaye *et al* (2017b).

Since fluorescence intensity provides a measure of the total amount of tubulin, we combine intensity measurements with simultaneous measurements of FRET fraction, which gives the fraction of tubulin in microtubules, to calculate the total amount of tubulin in microtubules. This is derived in Kaye *et al* (2017a), where the amount of donors in polymer (i.e. in microtubules), $N_{\mathrm{pol}}(x)$, was shown to be related to intensity and the fraction of donors engaged in FRET by:

$$N_{\mathrm{pol}}(x) = \frac{I(x)F(x)}{bP_f(1 + (a - 1)F(x))}, \tag{1}$$

where $F(x)$ is the fraction of donors engaged in FRET at location x, $I(x)$ is the intensity at location x, b is the average number of photons per donor not engaged in FRET, P_f is the probability a donor can engage in FRET and a is the relative brightness of donors engaged in FRET to donors not engaged in FRET. $F(x)$, a, and P_f are measured by FLIM and are unitless (experimental methods). Similarly, the monomer concentration (i.e. tubulin not in microtubules), $N_{\mathrm{mon}}(x)$, can be written as

$$N_{\mathrm{mon}}(x) = \frac{I(x)(P_f - F(x))}{bP_f(1 + (a - 1)F(x))}. \tag{2}$$

Thus, measuring both FRET (via FLIM) and fluorescence intensity in a spatially resolved manner provides a powerful tool to characterize the spindle interface.

2.2. Defining the spindle boundary and measuring the spindle microtubule concentration profiles

To measure microtubule concentration profiles, we first added donor- and acceptor-labeled tubulin to *Xenopus* egg extract containing metaphase spindles (experimental methods). We then imaged spindles and defined the spindle boundary by thresholding the intensity image. We note that the exact value used for defining the spindle boundary from the fluorescence image is somewhat arbitrary. However, the concentration profiles were insensitive to changing the value used in this definition and thus had little impact on the quantitative analysis which follows and no bearing on any of our main conclusions. Given this definition of the interface, we segmented the image into pixels that were equidistant from the spindle boundary (experimental methods, figure 3(A)). Pixels within the spindle boundary are defined to have a negative distance, while pixels outside the boundary are defined to have a positive distance. The pixels were then binned according to distance from the boundary and the photons corresponding to these pixels were analyzed to find the FRET fraction and intensity (figure 3(B)). The calculated FRET fraction was largest inside the spindle, i.e. to the negative values on the x-axis,

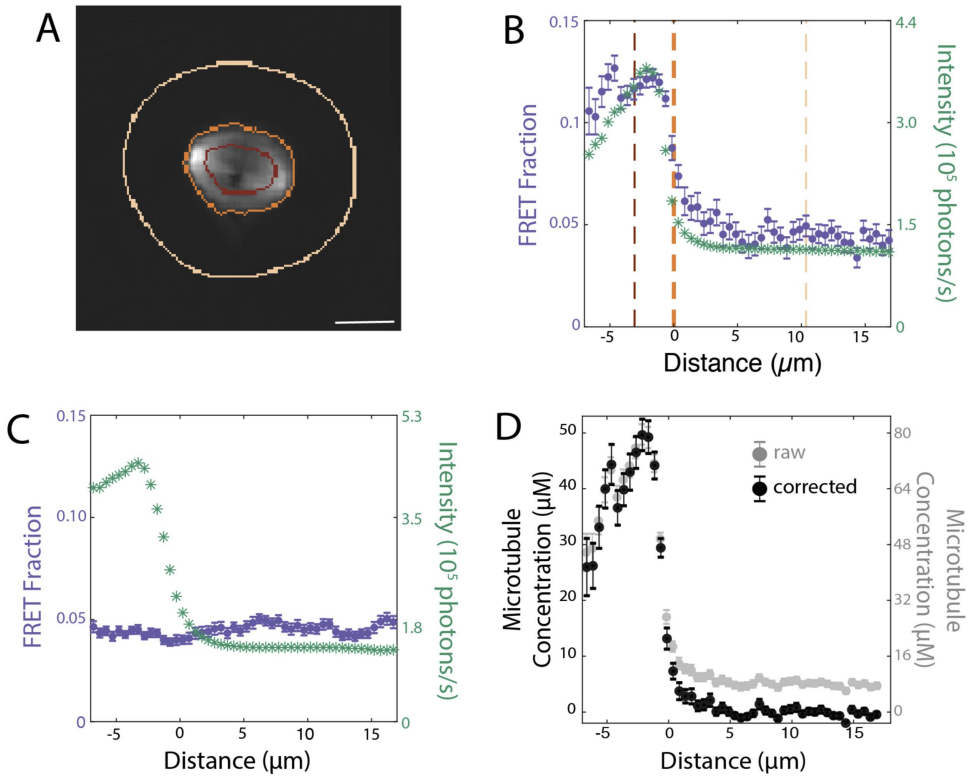

Figure 3. Microtubule concentration versus distance from spindle boundary. (A) Intensity image of spindle. The spindle boundary is shown in orange. Pixels are segmented into groups by their minimum distance from the spindle boundary. Select groupings are shown in light orange and dark orange. Scale bar is 10 μm. (B) FRET fraction (purple circles) and intensity (green stars) versus distance from grouped pixels. Error bars in FRET fraction are the standard deviation of the posterior distribution. Equidistant pixels are grouped together and the FRET fraction and intensity from each grouping is shown. Pixel groupings corresponding to -3.1 and $+10.4$ μm are marked by light orange and dark orange dashed lines, respectively. (C) FRET fraction and intensity versus distance from spindles ($n = 3$) formed without acceptor-labeled tubulin. Error bars in the FRET fraction are the standard deviation of the posterior distribution. The intensity profile is similar to (B) but FRET fraction is no longer increased in the spindle. This level of FRET fraction is used to estimate the bias in measured FRET fraction in (B). (D) Microtubule concentration versus distance without subtracting off bias (gray dots) and with subtracting off bias (black dots). Error bars are the standard deviation of the posterior distribution.

and rapidly decreased outside the spindle. Further than 5 μm away from the spindle—which is comparable to a typical MT length in the spindle—the FRET fraction had decayed to 0.044 ± 0.004, which is small but not zero. This finite FRET fraction measured far from the spindle might be caused by the presence of microtubules in solution far removed from the spindle, or it could be an artifact caused by errors in the FLIM measurement (perhaps due to mischaracterization of the instrument response function, auto-fluorescence of the *Xenopus* egg extract, or slight deviations of the donor lifetime distribution from a single exponential). To estimate the extent to which the calculated FRET fraction was due to actual FRET, we measured the intensity and FRET fraction from spindles that only contained donor-labeled tubulin (and thus could not produce FRET because of the absence of acceptor-labeled tubulin). Averaging FRET and intensity measurements from 3 spindles revealed a similar donor intensity profile to spindles with acceptor-labeled tubulin incorporated. In contrast, the calculated FRET fraction in the absence of acceptor-labeled tubulin was spatially uniform, with an average value of 0.046 ± 0.003. Since the donor-labeled tubulin cannot engage in FRET in the absence of acceptor-labeled tubulin, the spatially uniform calculated FRET fraction must be due to an artefactual offset. An artefactual offset in measured FRET fraction was previously seen with free dye in buffer (Kaye *et al* 2017a). To correct for this artifact, we averaged the FRET fraction over space in samples that lacked acceptor-labeled tubulin and used this value to correct the artefactual FRET fraction offset in samples with acceptor-labeled tubulin.

We then calculate a corrected polymer and monomer concentration using equations (1) and (2) and obtain:

$$N_{\mathrm{pol}}(x) = \frac{I(x)(F(x) - F_0)}{bP_f(1 + (a - 1)(F(x) - F_0))}, \tag{3}$$

$$N_{\mathrm{mon}}(x) = \frac{I(x)(P_f - (F(x) - F_0))}{bP_f(1 + (a - 1)(F(x) - F_0))}, \tag{4}$$

where F_0 is the artefactual offset a, the relative brightness of donors engaged in FRET to donors not engaged in FRET, was estimated from the ratio of the fluorescence lifetimes as previously described (Kaye *et al* 2017a). To

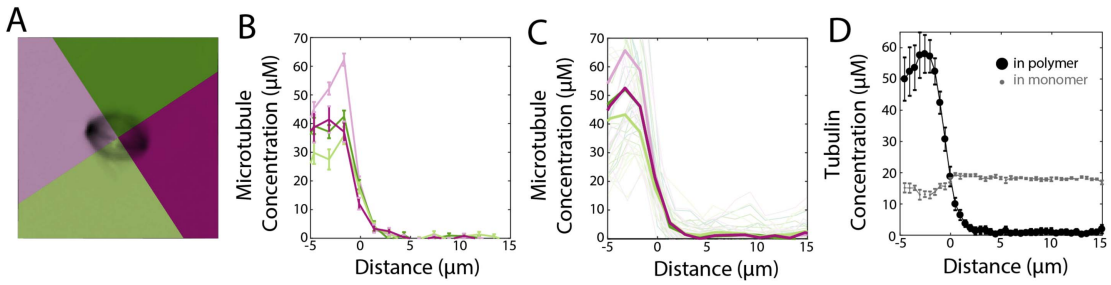

Figure 4. Microtubule concentration decays steeply and uniformly from the spindle boundary. (A) Intensity image of the spindle shown in figure 3 has been split up into quadrants. Two quadrants correspond to the poles (light red and dark red) and two correspond to the mid body (light green and dark green). Pixels are segmented into groups by their minimum distance from the spindle boundary in each quadrant. (B) Microtubule concentration curves from each quadrant shown in (A). Each quadrant is similar. Error bars are the standard deviation of the posterior distribution. (C) Microtubule concentration curves from each quadrant from 11 spindles. The averaged (opaque curves) and individual (non-opaque) Microtubule concentration curves show no obvious dependence on quadrant. (D) Microtubule concentration (large black circles) and the monomer concentration (small gray circles) as a function of distance from the spindle boundary are found using the FLIM/FRET technique described above. Results shown are the average of $N = 11$ spindles. Error bars are standard error of the mean.

determine b, the brightness of donors not engaged in FRET per μM tubulin, we measured the average intensity far from the spindle (>10 μm) and assume the tubulin concentration in this region to be 18 μM (Parsons and Salmon 1997, experimental methods). P_f is measured by grouping pixels by intensity, and then fitting the relationship between FRET and intensity as previously described (Kaye *et al* 2017a). We then calculated the microtubule concentration from the FRET and intensity measurements shown in figure 3(B) with and without the offset F_0 using equations (1) and (2), respectively (figure 3(D)). In both cases, we see that the concentration of tubulin in microtubules quickly decays from a maximum value in the spindle, to a low level away from the spindle. If the artefactual FRET offset was not corrected for, the microtubule concentration outside the spindle would be estimated to 8 μM $\pm$ 0.8 μM which corresponds to approximately 10% of its maximum value (figure 3(D), gray data-points). After correcting for the offset, the microtubule concentration we determine away from the spindle is -0.2 μM $\pm$ 0.7 μM (figure 3(D), black data-points). These measurements reveal that the microtubule concentration away from the spindle is less than our detection limit, which we estimated as 2 standard deviations of the concentration measurements, which is 1.4 μM. Combining this result with the findings that microtubule lifetimes are on the order of 20 s (Needleman *et al* 2010) indicate a negligible amount of the spontaneous nucleation of microtubules away from the spindle.

2.3. Microtubule and monomer concentration profiles are independent of the position along the spindle circumference

We next investigated if the shape of the concentration profile at the spindle interface varied between different locations along the surface of the spindle. For this analysis, we divided the spindle into quadrants (figure 4(A)). We grouped pixels by distance from the spindle boundary within each quadrant, as previously described. We calculated the microtubule concentration using equation (3) and found the microtubule concentration profile in each quadrant to be similar (figure 4(B)). This process was repeated for 11 spindles, revealing similar decay profiles for each quadrant (figure 4(C)). To quantitatively examine these curves, we use the half-width-at-half-max (HWHM) metric, which is defined as the distance between where the maximum of the curve lies and the point where the curve has decreased to one half its maximum value (figure 5(A) insert). Comparing the HWHM from poleward quadrants to lateral quadrants, we found that the decay length scale of the microtubule concentration profile at the interface was indistinguishable between these regions (two-sided paired-sample t-test, $p = 0.70$). Taken together, these results argue that the shape of the microtubule density profile around the spindle does not depend on the point along the circumference at which it is measured. Thus, we grouped pixels solely by their distance from the spindle boundary and calculated the microtubule and monomer concentration at each distance from the spindle boundary using equations (3) and (4), respectively. While the maximal microtubule concentration in the spindle is often larger for the poleward quadrants than lateral quadrants, more statistics are needed to make a definitive statement.

Since all the spindles displayed very similar microtubule decay profiles, we averaged the microtubule and monomer measurements from all spindles (figure 4(D)). The microtubule concentration quickly decays from 58 μM $\pm$ 6 μM to 0.8 μM $\pm$ 0.9 μM at 5 μm where error is estimated as standard error of the mean. The average microtubule concentration at distances larger than 5 μm, which is comparable to a typical microtubule length, is 0.9 μM $\pm$ 0.4 μM, where error is estimated as the standard deviation of the concentration measurements at each location between 5 and 15 μm. Monomer concentration is depleted from 14.7 μM $\pm$ 1.5 μM within the spindle to 18.3 μM $\pm$ 0.5 μM outside of the spindle (two-sample t-test with

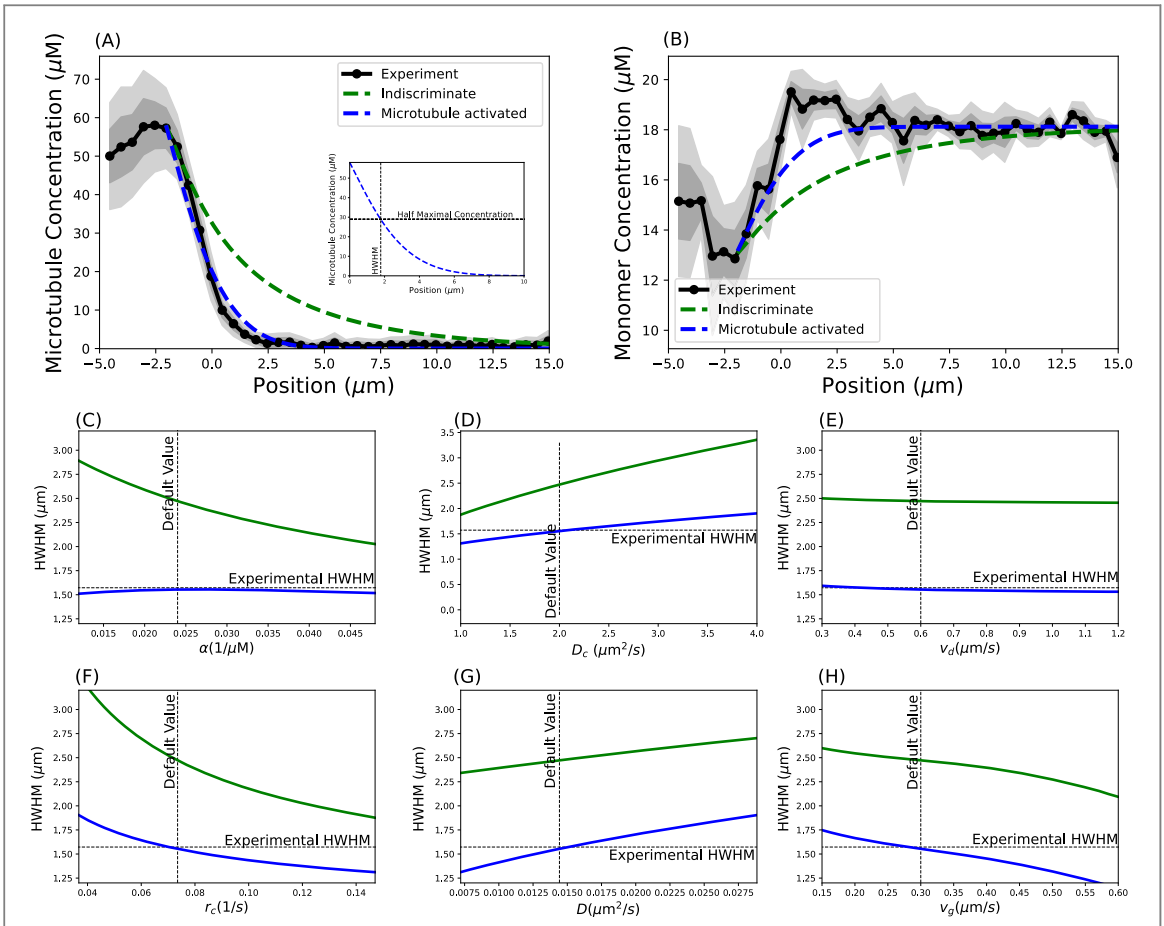

Figure 5. Comparisons of theory (dashed lines) and experiment (solid black line) for the concentration of tubulin in microtubules (A) and in monomer (B). The blue and green dashed lines show the limiting cases of $n_u = 0$ and $n_u = n_b$, respectively. One and two standard deviations of the data are shown in the dark and light gray regions, respectively. Microtubule activated nucleation (blue) much better describes the data than indiscriminate nucleation (green). We test the robustness of this finding by plotting the half-width-at-half-maximum of the interface HWHW defined in (insert A), for changing parameters α, D_c, v_g, r_c, D, v_g in (C)–(H), respectively. In the plots, the dotted lines show the parameters used in (A), (B) and the HWHM found in experiment (see appendix E).

unequal variances, $p = 0.000\,03$), where error is estimated as the variance between monomer values at each location. After obtaining the concentration of tubulin in microtubules, we then sought to construct models to investigate the expected concentration profile of microtubule concentration for different scenarios of nucleator activity.

3. Monomer and polymer concentration profiles at the spindle's interface from reaction diffusion dynamics

To better understand the measured concentration profiles near the spindle interface, we formulated a 1D model. Our model tracks the distribution of nucleators as function of the distance x from the spindle boundary and the distribution of microtubules as a function of x and their length l. The effects we consider are the spatial diffusion of nucleators in the presence of microtubules, the length dependent diffusion of microtubules themselves, and the growth dynamics of microtubules. We ignore active transport and advection of microtubules since the short lifetime of microtubules (about 20 s) does not allow for substantial transport at the velocities at which they typically move in the spindle (about 2 μm min^{-1} and mostly parallel to the spindle boundary). Given that the microtubule density profile at the spindle interface is independent of the position along the circumference of the spindle (see figure 4(A)) we also neglected the local curvature of the spindle in our modeling. Finally, for simplicity we did not track the orientational distribution of microtubules, which is negligible, since rotational diffusivity scales with the inverse of the third power of the polymer length, and in semi-dilute suspensions with the inverse of the second power of polymer concentration, (see Doi and Edwards 1988). Thus, we consider that microtubules which diffuse away from the interface stay parallel to it over their lifetime. In this section, we

Table 1. Summary of model parameters with their default values and sources. The first five parameters describe the nucleator dynamics, the latter six describe microtubule properties and dynamics.

D_c	Diffusivity of free nucleators	2 μm^2 s^{-1}	Lippincott-Schwartz *et al* (2001)
α	Binding affinity of nucleator to MT	0.024 μM^{-1}	Oh *et al* (2016)
r_c	Turnover rate of nucleator	$\frac{5}{4}r$	Estimate, see section 3.4
n_u	Nucleation activity of unbound nucleator	Adjustable	
n_b	Nucleation activity of bound nucleator	Adjustable	
D	Length dependent diffusivity of MTs	$D\ln(\epsilon/d)/\epsilon = D_c/10$	Estimate, see section 3.4
r	Turnover rate of MTs	1/17 s^{-1}	Brugués *et al* (2012)
v_g	MT growth velocity	0.3 μm s^{-1}	Brugués *et al* (2012)
v_d	MT depolymerization velocity	0.6 μm s^{-1}	Brugués *et al* (2012)
ε	Size of MT seed	50 nm	Estimate, see section 3.4
d	MT diameter	25 nm	Alberts *et al* (1983)

describe our model starting from a summary of the biochemical pathway of microtubule nucleation. All model parameters and their values are listed in table 1.

3.1. Chromosome-dependent microtubule nucleation

In metaphase *Xenopus* spindles, proteins in the nucleation pathway are inhibited from functioning by binding to importins. RanGTP interacts with these complexes, releasing the proteins and triggering microtubule nucleation (Kalab *et al* 1999, Ohba *et al* 1999, Zhang *et al* 1999, Melchior 2001). Ran is a small GTPase, which exists in either a GDP- or a GTP-bound state. RanGDP is converted to RanGTP by the GEF RCC1 at chromosomes, while RanGTP is converted to RanGDP by RanGAP1 in the cytoplasm. This gives rise to a narrow ($\simeq$3 μm) RanGTP gradient around the chromosomes (Kalab *et al* 2002, Caudron *et al* 2005, Maresca *et al* 2009, Hasegawa *et al* 2013, Oh *et al* 2016). This gradient has been speculated to give rise to the length scale of the spindle; however, recent experiments have shown that perturbing the length scale of the Ran gradient does not significantly alter the size of the spindle (Oh *et al* 2016). While RanGTP is essential for microtubule nucleation, it is not known whether there is a second level of regulation, namely whether nucleators need to bind to pre-existing microtubules in order to nucleate.

Closely following Oh *et al* (2016), we formulated a simple model for the dynamics of activated nucleators, denoted c_u and c_b if they are unbound or bound, respectively. In the bulk of the spindle, i.e. far from the RanGTP-enriched region around the chromosomes, the model reads

$$\partial_t c_u = D_c \partial_x^2 c_u - (\kappa\rho + r_c)c_u + \kappa_1 c_b, \tag{5}$$

$$\partial_t c_b = \kappa\rho c_u - (\kappa_1 + r_c)c_b, \tag{6}$$

where D_c is diffusivity of unbound nucleators, and r_c is their rate of rebinding importin and thus deactivating. Furthermore, κ and κ_1 are the binding and unbinding rate of nucleators to microtubules, respectively. Finally, ρ is the density of microtubules. Assuming that the binding–unbinding dynamics of nucleators are fast (see appendix C), $\kappa\rho c_u = \kappa_1 c_b$ and the dynamics of the total concentration of nucleators $c = c_u + c_b$ can be obtained from equations (5) and (6) and is given by,

$$\partial_t c = D_c \partial_x^2 \frac{c}{1 + \alpha\rho} - r_c c. \tag{7}$$

Here, $\alpha = \kappa/\kappa_1$ is the binding affinity of nucleator for microtubules. To find steady states, we will complement equation (7) with boundary conditions at the spindles interface where $c = c_s$ and at infinity where $c = c_\infty$, which will be discussed in section 3.3.

3.2. Microtubule equations of motion

We then developed a description of the growth, shrinkage, and diffusion dynamics of microtubules near the spindle interface. In our model, microtubules are nucleated from an initial size of ε, and grow at velocity v_g. They stochastically switch to a depolymerizing state at a rate of r. Depolymerizing microtubules shrink with a velocity v_d until they reach their initial size ε and disappear. All microtubules diffuse with a size-dependent diffusivity $D/\ell\ \ln(\ell/d)$ where ℓ is their current length and $d = 25$ nm is the diameter of a microtubule, (see Doi and Edwards 1988). Given this model, the polymer number densities of growing microtubules, $\psi_g(x,\ \ell)$, and shrinking microtubules, $\psi_d(x,\ \ell)$, obey

$$\partial_t \psi_g(x,\ \ell) = -v_g \partial_\ell \psi_g + \frac{D}{\ell} \ln\left(\frac{\ell}{d}\right) \partial_x^2 \psi_g - r\psi_g \tag{8}$$

and

$$\partial_t \psi_d(x,\ \ell) = v_d \partial_\ell \psi_d + \frac{D}{\ell} \ln\left(\frac{\ell}{d}\right) \partial_x^2 \psi_d + r\psi_g. \tag{9}$$

The structure of equations (8), (9) is as follows: the first term on the right-hand side describes the growth dynamics of MTs. The second term describes their length dependent diffusion using the form derived for elongated rods (Doi and Edwards 1988). The last term describes their switching from a growing to a shrinking state. For simplicity, we ignore the effects of rotational diffusion since rotational diffusivity scales with the inverse of the third power of polymer length and, in semi-dilute suspensions, with the inverse of the second power of polymer concentration (see Doi and Edwards 1988). We also neglect active transport of microtubules by direct interactions between MTs. This is justified since microtubules in spindles—given typical sliding velocities of 2 μm min^{-1} and lifetimes of 20 s—typically move less than 1 μm.

The mass density of polymer is given by

$$\rho = \int_\varepsilon^\infty (\psi_g + \psi_\mathrm{d})\ell \mathrm{d}\ell \tag{10}$$

and obeys

$$\dot{\rho} = \varepsilon(v_g\psi_g - v_\mathrm{d}\psi_\mathrm{d})|_{\ell=\epsilon} + \int_\varepsilon^\infty (v_g\psi_g - v_\mathrm{d}\psi_\mathrm{d})\mathrm{d}\ell. \tag{11}$$

In equation (11) the first term $\varepsilon(v_g\psi_g - v_d\psi_d)|_{\ell=\epsilon}$ captures the gain and loss of polymer mass by nucleation and disassembly of microtubules, while the second term $\int_\varepsilon^\infty (v_g\psi_g - v_\mathrm{d}\psi_\mathrm{d})\mathrm{d}\ell$ describes the effect of (de) polymerization dynamics on the microtubule mass. Nucleation enters our equations of motion via the boundary condition

$$\varepsilon v_g \psi_g(x,\ \ell)|_{\ell=\varepsilon} = m(x), \tag{12}$$

where the locally nucleated microtubule mass $m(x)$ obeys

$$m(x) = c\frac{n_u + \alpha\rho n_b}{1 + \alpha\rho}, \tag{13}$$

where c is density of nucleators, n_b is the rate of nucleation by bound nucleators and n_u is the rate of nucleation by unbound nucleators. To obtain this expression, we used the fact that the concentration of bound and unbound nucleators is given by $\frac{c\,\alpha\rho}{1+\alpha\rho}$ and $\frac{c}{1+\alpha\rho}$, respectively.

3.3. Boundary conditions at the spindle interface and far away

To find the steady states of equations (7)–(9), we applied boundary conditions at the spindle interface and at infinity. Far from the spindle, all nucleators are presumed inactive and thus

$$c_\infty = 0, \tag{14}$$

where $c_\infty = c|_{x\to\infty}$. This implies that any microtubules far from the spindle originated from spontaneous nucleation—which we take to be zero here—and thus

$$\varepsilon v_g \psi_g|_{x\to\infty,\ell=\varepsilon} = 0 \tag{15}$$

which implies that

$$\psi_g|_{x\to\infty} = \psi_d|_{x\to\infty} = 0. \tag{16}$$

We next discuss the boundary condition to the inside of the spindle at $x = 0$. Inside the spindle, we assume a constant density of microtubules $\rho = 1$, which normalizes all densities of growing and shrinking microtubules at $x = 0$, which we denote ψ_g^s and ψ_d^s, respectively. They obey

$$\psi_g^s = \frac{r^2 v_d}{v_g(\epsilon r + v_g)(v_d + v_g)} \exp\left(-\frac{r}{v_g}(\ell - \epsilon)\right), \tag{17}$$

$$\psi_d^s = \frac{r^2}{(\epsilon r + v_g)(v_d + v_g)} \exp\left(-\frac{r}{v_g}(\ell - \epsilon)\right). \tag{18}$$

Using equation (12), we solve for the concentration of nucleators c_s in the spindle and find

$$c_s = \frac{\epsilon r^2 v_d(\alpha + 1)}{(v_d + v_g)(\alpha n_b + n_u)(\epsilon r + v_g)}, \tag{19}$$

which is the boundary condition for the concentration at $x = 0$.

3.4. Microtubule activated nucleation best explains experiments

We next sought to use our model to answer the main question of this paper: are nucleators activated by binding to pre-existing microtubules or are they active irrespective of their binding state?

We fixed parameters of the model using measurements from the literature wherever possible. The dynamics of microtubules in the spindle are well characterized. Using the average lifetime of microtubules, we infer the average rate of switching from polymerizing to depolymerizing to be $r = \frac{1}{17}\ \mathrm{s}^{-1}$ (Brugués *et al* 2012). In conjunction with the average microtubule length of 6 μm, we estimate the microtubule growth velocity to be $v_g = 0.3\ \mu\mathrm{m\ s}^{-1}$. From measurements taken in Brugués *et al* (2012), we set the microtubule depolymerization velocity to be $v_d = 0.6\ \mu\mathrm{m\ s}^{-1}$.

The properties of nucleators are poorly understood and even the proteins responsible for nucleation are still under debate. Here we do not commit to a specific nucleator. For the nucleators diffusivity we choose $D_c = 2\ \mu\mathrm{m}^2\ \mathrm{s}^{-1}$, which corresponds to the diffusion of γTuRC (Lippincott-Schwartz *et al* 2001) in the cytoplasm. This is a reasonable lower bound and places us in a limit where differences between our two models will be least pronounced (see also figure 5(D)). For the binding affinity of the nucleator to microtubules, we take the value estimated for the molecule HSET in Oh *et al* (2016) of $\alpha = 0.024\ \mu\mathrm{M}^{-1}$.

We set $r_c = 1.25\ r$, the rate at which the nucleator becomes deactivated, slightly higher than the microtubule catastrophe rate. This value produces the best fit for the measured microtubule concentration profile at the interface. Finally, we set the smallest size of a microtubule $\epsilon = 50$ nm, which is about twice the microtubule diameter, and set this smallest piece to diffuse with a diffusion coefficient of $D\ \ln(\epsilon/d)/\epsilon = D_c/10$, which defines the length dependent diffusivity D in equations (8), (9).

Using these parameters, we numerically obtained steady state solutions to the system of equations (7)–(9) with the boundary conditions defined by equations (12)–(16). The numerical procedure is outlined in appendix D. We then compared the microtubule and monomer concentration profile shapes at the interface generated by the model to experimental measurements (figures 5(A) and (B), black line). We numerically tested two limiting cases $n_u/n_b = 1$ (indiscriminate nucleation, green curve) and $n_u/n_b = 0$ (microtubule-activated nucleation, blue curve.) We find that the microtubule concentration profiles are better approximated by the microtubule-activated nucleation model, see figure 5(A). From our model, we furthermore predicted monomer concentration profiles using that the total flux of tubulin vanishes in steady state, i.e. $c_m = -\frac{D}{D_m}\int_{\varepsilon}^{+\infty} \ln\left(\frac{\ell}{\mathrm{d}}\right)(\psi_g + \psi_\mathrm{d})\,\mathrm{d}\ell + c_m^{\infty}$, where c_m and D_m pertain to the concentration and diffusivity of tubulin monomer, respectively. Taking c_m^{∞}, the monomer concentration at infinity, directly from data and using $D_m = D_{MT}/1.3$, which best fits the data, we find that the experimental monomer concentration profiles are best approximated by the microtubule activated nucleation model as well, see figure 5(B).

To test the robustness of these findings, we explored a range of parameters around our estimated values and quantified how the half-width-at-half-maximum (HWHM, see figure 5(C)) of interfaces in experiments would change upon tuning parameters of the model. This is displayed in figures 5 (D)–(H), in which the colored solid lines display the HWHM for different ratios n_u/n_b. The dashed lines mark the parameter estimate used in (A) and (B) and the HWHM estimated from experimental data (see appendix E). Tuning all parameters of the model between half and twice initial estimates we find that microtubule-activated nucleation robustly predicts the sharpest interface. It is noteworthy that the difference between the two models gets less pronounced as the binding affinity of nucleator to microtubules α increases because unbound nucleators become rare for high α. However, both models stay distinct until α increases to about an order of magnitude higher than its value estimated in Oh *et al* (2016). Moreover, we tested whether our conclusions were robust to other effects that microtubule binding could have on the behavior of nucleators. In particular, we considered what would happen if microtubule binding changed the lifetime of the nucleator, i.e. bound nucleators might tend to deactivate less than unbound ones. We reformulated our model to incorporate this possibility and did not find a marked difference between the two cases (appendix B). Finally, we asked whether adding transport to our model would change our conclusions. We thus tested numerically whether including a transport term that deterministically moved microtubules towards the spindle interface would change our findings. We found even upon inclusion of such a transport term, with a velocity of up to 2.5 μm min^{-1} (Kinesin sliding velocity) towards the spindle, only the microtubule activated nucleation model could explain the narrow interface experimentally observed (data not shown). Taken together, our results strongly suggest that nucleators are activated by pre-existing microtubules.

4. Discussion

Spindle microtubules are nucleated by accessory proteins whose activity is spatially regulated. In this paper, we investigated the spindle interface to learn about the microtubule nucleation mechanism which maintains the

spindle as a well-separated structure in the cell. In particular, we investigated whether nucleators binding to pre-existing microtubules stimulate their activity.

To do this, we utilized a polymer measurement technique previously described (Kaye *et al* 2017a) to measure microtubule concentration around the spindle boundary. We measured the microtubule concentration profiles near the interface in 11 spindles and found that the microtubule concentration decays sharply at the boundary. The length scale of the decay was indistinguishable between spindles and between poleward and mid-body quadrants of each spindle.

To interpret these results, we formulated a model for diffusing and growing microtubules near the spindle interface. By comparing the predicted and measured microtubule concentration profiles at the spindle interface, we found that the data was consistent with nucleators being activated by binding to pre-existing microtubules and inconsistent with nucleators being unaffected by their binding state. We conclude that the rate of microtubule nucleation increases when nucleators bind microtubules. It is noteworthy that the measured microtubule concentration profile is steeper than the model predicts, and unlike the model, it has both concave and convex parts. This discrepancy may be due to microtubule interactions in the spindle from motor proteins or other crosslinkers, which are not included in the model. Previous work has shown that dynein can exert isotropic contractile stresses in metaphase extracts, which could explain the difference between the model and the data (Foster *et al* 2015, Foster *et al* 2017).

The conclusions of this study are based on measuring and modeling concentration profiles of microtubules and tubulin in and around spindles and will hold independent of the precise biochemical pathway of nucleation, which is yet to be established. The very sharp decay of the concentration profile of microtubules at the spindle interface argues that the activity of microtubule nucleators is strongly enhanced upon binding microtubules. As microtubule nucleators must first be activated by the Ran pathway (Kalab *et al* 1999, Ohba *et al* 1999, Zhang *et al* 1999), this suggests that the activation of nucleators is a two-step process: inactive nucleators in the cytoplasm are first primed by proximity to chromosomes (by the Ran pathway), but only become fully activated after the primed nucleators bind to microtubules (Clausen and Ribbeck 2007, Goshima *et al* 2008, Decker *et al* 2018). An important challenge for the future is to establish the molecular basis by which microtubules activate microtubule nucleators.

Different organelles in cells maintain chemically and mechanically distinct micro-environments, even though many of them, like the spindle, are not enclosed by a membrane to separate them from their surroundings. One mechanism of maintaining such sharp compartment boundaries within a common cytoplasm is phase separation, which has recently been a central point of interest for many cell biologists and biophysicists (Brangwynne *et al* 2009, Decker *et al* 2011, Zwicker *et al* 2014). The nucleation mechanisms we study here points towards an alternative possibility for achieving a similar result. Distinct structures can also be maintained by providing a scaffold via spatially regulated nucleation, in which the nucleation product feeds back on the activity of the nucleator. The *Xenopus* meiotic spindle is an intriguing and biologically important example of this mechanism at play. Future work will be needed to explore whether nucleation-feedback mechanisms are equally ubiquitous as non-equilibrium liquid–liquid phase separations for cellular compartmentalization.

Acknowledgments

We thank Jess Crossno, Emily Davis, and Jan Brugues for thoughtful discussion. BK thanks FAS Division of Science, Research Computing Group at Harvard University for access to the Odyssey cluster. BK was supported by National Science Foundation GRFP Fellowship DGE1144152. DN acknowledges the Kavli Institute for Bionano Science and Technology at Harvard University, United States–Israel Binational Science Foundation Grant BSF 2009271, and National Science Foundation grants PHY-1305254, PHY-0847188, DMR-0820484, and DBI-0959721. Furthermore, this work was partially funded by NSF Grants DMR-1420073 (NYU MRSEC: MS), DMS-1463962 (MS), DMS-1620331 (MS), NIH Grant GM104976 (MS and DN).

Appendix A. Experimental methods

A.1. Sample preparation

Samples were measured in a conventional flow cell sealed by candlewax. Bovine tubulin was purified and then labeled with fluorophores as previously described (Mitchison and Kirschner 1984, Hyman *et al* 1991, Mitchison Lab 2012). Spindles were assembled in *Xenopus* laevis egg extracts as previously described (Hannak and Heald 2006). Tubulin was added to egg extracts by adding donor-labeled tubulin to 0.6 μM and acceptor-labeled tubulin to 1.9 μM. Atto565 was used as the donor fluorophore and Atto647N was used as the acceptor fluorophore.

A.2. Microscopy

Our microscope system was constructed around an inverted microscope (Eclipse Ti, Nikon, Tokyo, Japan) with a commercial scanning system (DCS-120, Becker and Hickl, Berlin, Germany). Fluorophores are excited with a Ti:sapphire pulsed laser (Mai-Tai, Spectra-Physics, Mountain View, CA) at a 1000 nm wavelength, 80 MHz repetition rate (70 fs pulse width), and emitted photons are detected with hybrid detectors (HPM-100-40, Becker and Hickl). The excitation laser was collimated by a telescope assembly to fully utilize the numerical aperture of a water-immersion objective (CFI Apo 40 WI, NA 1.25, Nikon) and avoid power loss at the XY galvanometric mirror scanner. The fluorescence from samples was imaged with a non-descanned detection scheme with a dichroic mirror (705 LP, Semrock) to allow the excitation laser beam to excite the sample while fluorescence passed into the detector path. A short-pass filter was used to further block the excitation laser beam (720 SP, Semrock), followed by an emission filter appropriate for Atto565-labeled tubulin (590/30 nm BP, Semrock).

A.3. Acquiring photon arrival-time histograms

We use a Becker and Hickl Simple-Tau 150 FLIM system to collect photon arrival-time histograms. Arrival times are measured relative to an electric pulse created by a photodiode that is triggered by the excitation laser (Becker 2010). The TAC range was set to 7×10^{-8}, with a gain of 5, corresponding to a 14 ns maximum arrival-time. The TCSPC system can lose fidelity for photons that arrive just before or after the excitation of the photodiode (Becker 2010), and thus we set the lower and upper limits to 10.59 and 77.25, respectively, resulting in a 10 ns recording interval. The instrument response was measured using fixed-point illumination of second harmonic generation of a urea crystal. The intensity of the illumination beam was set such that there was an average of 200 000–300 000 photons per second recorded. Data was acquired as a 128×128 pixel image, where a corresponding photon arrival-time histogram was recorded for each pixel.

A.4. Data analysis

Estimating the FRET fraction and Intensity from Photon Arrival Histograms: we use a Bayesian model to build posterior distributions from photon arrival-time histograms (Kaye *et al* 2017a). The posterior was evaluated at uniformly spaced grid points in parameter space. Point estimates of the FRET fraction were found by taking the maximum of the posterior distribution of the FRET fraction. To reduce the number of free parameters when analyzing photon arrival histograms to find the FRET fraction, we first found the two lifetimes of the donor fluorophore, and then fixed those lifetimes in our Bayesian analysis. Those ratio of those two lifetimes were used to estimate a, the relative brightness of fluorophores engaged in FRET to those not engaged in FRET. Pf was found in each sample as previously described (Kaye *et al* 2017a). The intensity was corrected for inhomogeneous illumination intensity.

Image registration: to collect a sufficient number of photons for FLIM analysis of FRET, spindles were required to be imaged for 100 s. An acquisition for this duration produces blurry images. Thus, we acquired multiple 10 s acquisitions of spindles and aligned the acquisitions as previously described (Brugués *et al* 2010). In short, intensity images are thresholded to include the spindle region. The resulting images are then translated so that the center of mass is centered within the image. Each image is then rotated such that the normalized autocorrelation with the previous frame is maximized. After rotation, the images are translated once more such that the normalized autocorrelation is maximized. Translation and rotation were done using the MATLAB (R2017a) function imtranslate (with linear interpolation) and imrotation (with no interpolation), respectively.

Image segmentation: registered images were segmented by thresholding the spindle to find the boundary of the spindle. Pixels are then segmented into groups by the shortest distance between the pixel and the spindle boundary. Pixels inside the boundary are considered to have a negative distance and pixels outside the spindle are considered to have a positive distance. The photon arrival-time histograms corresponding to each pixel in a group were added together to create the photon arrival-time histogram corresponding to that distance from the spindle boundary. The intensity of this group is calculated as the mean intensity of the pixels in the group.

Finding b in equations (3) and (4): we solve for b, the brightness per μM tubulin, by setting N_{mon} far from the spindle (>1 μm from the spindle boundary) to be 18 μM. This calculation assumes that the microtubule concentration in this region is negligible, as is consistent with our findings that polymer concentration is indistinguishable from 0 in this region (figures 3(D) and 5(D)). When we do not make this assumption by setting N_{pol} and N_{mon} equal to 18 M far from the spindle, we see very similar microtubule and monomer concentration curves.

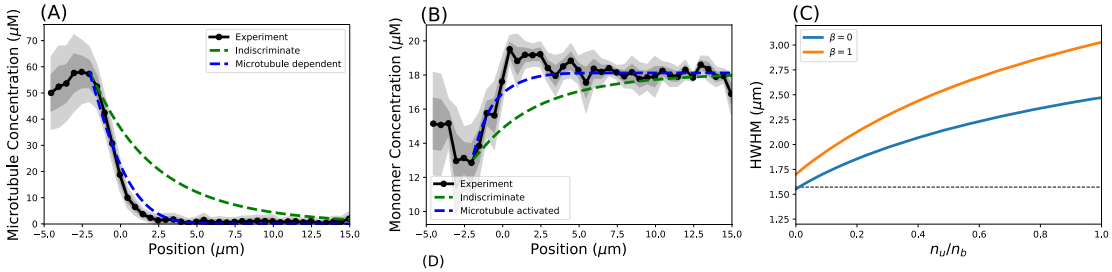

Figure B1. Comparisons of theory (dashed lines) and experiment (solid black line) for the microtubule concentration (A) and the monomer concentration (B), for $\beta = 1$. The blue and green dashed lines show the limiting cases of $n_u = 0$ and $n_u = n_b$, respectively. One and two standard deviations of the data are shown in the dark and light gray regions, respectively. The case of microtubule activated nucleation (blue) much better describes the data than indiscriminate nucleation (green). Irrespective of β the microtubule activated nucleation produces the sharpest HWHW (C), which corresponds most closely to experiments.

Appendix B. Binding dependent nucleator deactivation

To further probe the robustness of our model we formulated an extension in which we allowed the deactivation of nucleators to depend on their binding state. In this extended model

$$\partial_t c_u = D_c \Delta c_u - (\kappa\rho + r_c) c_u + \kappa_1 c_b \,, \tag{B1}$$

$$\partial_t c_b = \kappa\rho c_u - \kappa_1 c_b - r_c(1-\beta) c_b, \tag{B2}$$

where β is dimensionless and varies from 0 to 1 which describes whether bound nucleators are protected from being deactivated ($\beta = 1$) or turn over like unbound ones ($\beta = 0$). Assuming, like for the model in the main text, that the binding–unbinding dynamics of nucleators is fast (see appendix C), $\kappa\rho c_u = \kappa_1 c_b$ and the dynamics of the total concentration of nucleators $c = c_u + c_b$ can be obtained from equations (B2) and (B1) and is given by,

$$\partial_t c = D_c \partial_x^2 \frac{c}{1+\alpha\rho} - r_c \left(1 - \frac{\beta}{1+\alpha\rho}\right) c. \tag{B3}$$

In figure B1 we show that regardless of β our finding that the interfaces shape is consistent with MT activated nucleation, but not with MT independent nucleation.

Appendix C. Fast binding limit of nucleation

To derive the fast time scale limit of our nucleation model we introduce $P = \alpha\rho c_u - c_b$, which obeys, according equations (5) and (6)

$$\partial_t P = \alpha\rho D \Delta c_u - (\kappa\rho + \kappa_1 + r_c) P, \tag{C1}$$

which by introducing $\varepsilon = \frac{1}{\kappa\rho + \kappa_1 + r_c}$, can be rewritten as

$$\partial_t (\mathrm{e}^{-\frac{t}{\varepsilon}} P) = \mathrm{e}^{-\frac{t}{\varepsilon}} \alpha\rho D \Delta c_u \tag{C2}$$

and has the solution

$$P(t) = \mathrm{e}^{-\frac{t}{\varepsilon}} P_{-\infty} + \varepsilon \int_{-\infty}^{t} \frac{\mathrm{d}s}{\varepsilon} \mathrm{e}^{-\frac{(t-s)}{\varepsilon}} \alpha\rho D \Delta c_u \approx 0 + \mathcal{O}(\varepsilon). \tag{C3}$$

Thus, in the limit $\kappa\rho + \kappa_1 + r_c \to \infty$

$$\kappa\rho c_u = \kappa_1 c_b. \tag{C4}$$

Appendix D. Numerical implementation of the model

We numerically determine the shapes of the concentration profiles of polymer and monomers at the interface of the spindle. Our procedure is as follows: given a guess of the microtubule density ρ_1 we determine a corresponding nucleator density c_1 by solving equation (7) with the boundary conditions equations (19) and (14) using a second order finite difference scheme. Note, here and in the following the index one denotes a specific guess for the concentration and the quantities devolving from it. Given c_1 and ρ_1 the spatial distribution of nucleation events $M_1(x)$ is given by solving equation (13). We next determine the distribution $\psi_g^{(1)}$, by

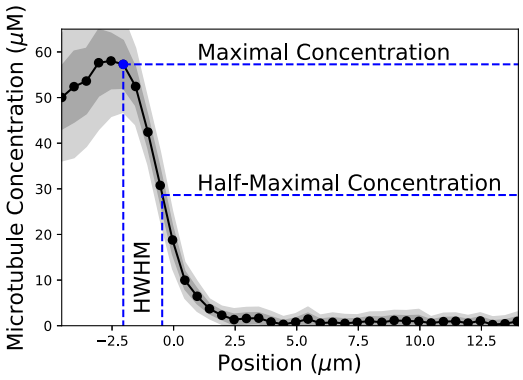

Figure E1. Illustration of the procedure for defining a HWHM for the interface from the data. We measure the distance at which the microtubule concentration has decayed to half the value it had at the first point from which the concentration profile started decaying.

integrating equation (8) along the ℓ direction, using equation (12) to set the initial condition at $\ell = \varepsilon$. The integration is performed using scipys odeint integration routine. Using the same technique, we also determine $\psi_d^{(1)}$. The steady state solution obeys the fixed-point equation

$$F(\rho_1) = \int_{\varepsilon}^{\infty} \ell(\psi_g^{(1)} + \psi_{\mathrm{d}}^{(1)})\mathrm{d}\ell - \rho_1 = 0. \tag{D1}$$

We find the roots of $F(\rho)$ using Broyden's method.

To compare numerical and experimental data, we align the numerical profile with the first experimental data point for which the microtubule concentration has started to decrease.

Appendix E. Characterizing the width of the polymer gradient

To compare the width of experimentally measured and numerically determined interfaces, we characterize the width of the spindles interface by reporting the distance from the first experimental data point in the interface, which is defined as the first datapoint at which the microtubule concentration has started to decrease, to the point where the concentration has decreased to half its that value. This procedure is illustrated in figure E1 and is identical to the method used for extracting a width measure from our numerical results, (see figure 5(A), insert).

ORCID iDs

Peter J Foster https://orcid.org/0000-0003-1818-5886
Sebastian Fürthauer https://orcid.org/0000-0001-9581-5963

References

Alberts B, Bray D, Lewis J, Raff M, Roberts K and Watson J D 1983 *Molecular Biology of the Cell* (New York: Garland)
Becker W 2010 *The bh TCSPC Handbook* (Berlin: Becker and Hickl)
Brangwynne C P, Eckmann C R, Courson D S, Rybarska A, Hoege C, Gharakhani J, Julicher F and Hyman A A 2009 *Science* **26** 1729–32
Brugués J and Needleman D J 2010 Nonequilibrium fluctuations in metaphase spindles: polarized light microscopy, image registration, and correlation functions *Proc. SPIE.* **7618** 76180L
Brugués J, Nuzzo V, Mazur E and Needleman D J 2012 Nucleation and transport organize microtubules in metaphase spindles *Cell* **149** 554–64
Caudron M, Bunt G, Bastiaens P and Karsenti E 2005 Spatial coordination of spindle assembly by chromosome-mediated signaling gradients *Science* **309** 1373–6
Clausen T and Ribbeck K 2007 Self-organization of anastral spindles by synergy of dynamic instability, autocatalytic microtubule production, and a spatial signaling gradient *PLoS One* **2** e244
Decker F, Oriola D, Dalton B and Brugues J 2018 Autocatalytic microtubule nucleation determines size and mass *Xenopus Laevis* egg extract of spindles *eLife* **7** e31149
Decker M, Jaensch S, Pozniakovsky A, Zinke A, O'Connell K F, Zachariae W, Myers E and Hyman A A 2011 Limiting amounts of centrosome material set centrosome size in C.elegans embryos *Curr. Biol.* **21** 1259–67
Doi M and Edwards S F 1988 *The Theory of Polymer Dynamics* (vol 73) (Oxford: Oxford university Press)
Foster P J, Fürthauer S, Shelley M J and Needleman D J 2015 Active contraction of microtubule networks *eLife* **4** e10837
Foster P J, Yan W, Fürthauer S, Shelley M and Needleman D J 2017 Connecting macroscopic dynamics with microscopic properties in active microtubule network contraction *New J. Phys.* **19** 125011
Goshima G, Mayer M, Zhang N, Stuurman N and Vale R D 2008 Augmin: a protein complex required for centrosome-independent microtubule generation within the spindle *J. Cell Biol.* **181** 421–9

Hannak E and Heald R 2006 Investigating mitotic spindle assembly and function invitro using Xenopus laevis egg extracts *Nat. Protoc.* **1** 2305–2314

Hasegawa K, Ryu S J and Kalab P 2013 Chromosomal gain promotes formation of a steep RanGTP gradient that drives mitosis in aneuploid cells *J. Cell Biol.* **200** 151–61

Ho Kimmy C-M, Hotta T, Kong Z, Tracy Zeng C J, Sun J, Julie Lee Y-R and Liu B 2011 Augmin plays a critical role in organizing the spindle and phragmoplast microtubule arrays in arabidopsis *Plant Cell* **23** 2606–18

Hsia K-C, Wilson-Kubalek E M, Dottore A, Hao Q, Tsai K-L, Forth S, Shimamoto Y, Milligan R A and Kapoor T M 2014 Reconstitution of the augmin complex provides insights into its architecture and function *Nat. Cell Biol.* **16** 852–63

Hyman A, Drechsel D, Kellogg D, Salser S, Sawin K, Steffen P, Wordeman L and Mitchison T 1991 [39] Preparation of modified tubulins *Methods Enzymol.* **96** 478–85

Ishihara K, Korolev K S and Mitchison T J 2016 Physical basis of large microtubule aster growth *eLife* **5** e19145

Ishihara K, Nguyen P A, Groen A C, Field C M and Mitchison T J 2014 Microtubule nucleation remote from centrosomes may explain how asters span large cells *Proc. Natl Acad. Sci. USA* **111** 17715–22

Kalab P, Pu R T and Dasso M 1999 The Ran GTPase regulates mitotic spindle assembly *Curr. Biol.* **9** 481–4

Kalab P, Weis K and Heald R 2002 Visualization of a Ran-GTP gradient in interphase and mitotic Xenopus egg extracts *Science* **295** 2452–6

Kamasaki T, O'Toole E, Kita S, Osumi M, Usukura J, Richard McIntosh J and Goshima G 2013 Augmin-dependent microtubule nucleation at microtubule walls in the spindle *J. Cell Biol.* **202** 25–33

Kaye B, Peter J F, Yoo T Y and Needleman D J 2017a Developing and testing a bayesian analysis of fluorescence lifetime measurements *PLoS One* **12** e0169337

Kaye B, Yoo T Y, Foster P J, Yu C-H and Needleman D J 2017b Bridging length scales to measure polymer assembly *Mol. Biol. Cell* **28** 1379–88

Lippincott-Schwartz J, Snapp E and Kenworthy A 2001 Studying protein dynamics in living cells *Nat. Rev. Mol. Cell Biol.* **2** 444–56

Maresca T J, Groen A C, Gatlin J C, Ohi R, Mitchison T J and Salmon E D 2009 Spindle assembly in the absence of a RanGTP gradient requires localized CPC activity *Curr. Biol.* **19** 1210–5

Melchior F 2001 Ran GTPase cycle: one mechanism two functions *Curr. Biol.* **11** R257–60

Mitchison T 2012 Labeling tubulin and quantifying labeling stoichiometry https://mitchison.hms.harvard.edu/files/mitchisonlab/files/labeling_tubulin_and_quantifying_labeling_stoichiometry.pdf?m=1446057507 (Accessed: 22 May 2017)

Mitchison T and Kirschner M 1984 Microtubule assembly nucleated by isolated centrosomes *Nature* **312** 232–7

Needleman D J, Groen A, Ohi R, Maresca T, Mirny L and Mitchison T 2010 Fast microtubule dynamics in meiotic spindles measured by single molecule imaging: evidence that the spindle environment does not stabilize microtubules *Mol. Biol. Cell* **21** 323–33

Oh D, Yu C-H and Needleman D J 2016 Spatial organization of the ran pathway by microtubules in mitosis *Proc. Natl Acad. Sci.* **113** 8729–34

Ohba T, Nakamura M, Nishitani H and Nishimoto T 1999 Self-organization of microtubule asters induced in Xenopus egg extracts by GTP-bound ran *Science* **284** 1356–8

Parsons S F and Salmon E D 1997 Microtubule assembly in clarified Xenopus egg extracts *Cell Motil. Cytoskeleton* **36** 1–11

Petry S, Aaron C G, Ishihara K, Mitchison T J and Vale R D 2013 Branching microtubule nucleation in Xenopus egg extracts mediated by augmin and TPX2 *Cell* **152** 768–77

Roll-Mecak A and Vale R D 2006 Making more microtubules by severing: a common theme of noncentrosomal microtubule arrays? *J. Cell Biol.* **175** 849–51

Sawin K E 1991 Poleward microtubule flux mitotic spindles assembled *in vitro J. Cell Biol.* **112** 941–54

Wieczorek M, Bechstedt S, Chaaban S and Brouhard G J 2015 Microtubule-associated proteins control the kinetics of microtubule nucleation *Nat. Cell Biol.* **17** 907–16

Zhang C, Hughes M and Clarke P R 1999 Ran-GTP stabilizes microtubule asters and inhibits nuclear assembly in Xenopus egg extracts *J. Cell Sci.* **112** 2453–61

Zwicker D, Decker M, Jaensch S, Hyman A A and Jülicher F 2014 Centrosomes are autocatalytic droplets of pericentriolar material organized by centrioles *Proc. Natl Acad. Sci. USA* **111** E2636–45